Eccentricity forcing on Tropical Ocean Seasonality

Luc Beaufort[1] and Anta Clarisse Sarr[2]

[1]Aix-Marseille Univ., CNRS, IRD, INRAE, CEREGE, 13090 Aix-en-Provence, France
[2]Univ. Grenoble Alpes, Univ. Savoie Mont Blanc, CNRS, IRD, Univ. Gustave Eiffel, ISTerre, 38000 Grenoble, France

Correspondence: Luc Beaufort (beaufort@cerege.fr)

Abstract. The amount of radiative energy received at the Earth's surface depends on two factors: Earth-Sun distance and sunlight angle. Because of the former factor, high eccentricity cycles can induce the appearance of seasons in the tropical ocean. In this paper, we use the Earth System model IPSL-CM5A2 to investigate the response of the low-latitude oceans to variations in Earth's orbital eccentricity. Sea Surface Temperature (SST) and Primary Production (PP) were simulated under

5 six precession configurations at high eccentricity and two configurations with low eccentricity, representing extreme configurations observed over the past million years. Results show that high eccentricity leads to increased seasonality in SST, with an annual thermal amplitude of approximately 2.2°C in low latitude ocean surface waters (vs. 0.5°C at low eccentricity). PP, which already exhibits inherent seasonality under low eccentricity conditions, sees its seasonality largely increased under high eccentricity. As a consequence, we show that on long time scales the intensity of SST seasonality exhibits only the eccentricity

10 frequency, whereas that of PP additionally follows precession dynamics. Furthermore, the seasonal variations in both SST and PP at high eccentricities are influenced by the annual placement of perihelion with its direct impact of radiative energy received in tropical regions. This leads to a gradual and consistent transition of seasons within the calendar. We introduce the concept of "eccentriseasons," referring to distinct annual thermal differences observed in tropical oceans under high eccentricity conditions, which shift gradually throughout the calendar year. These findings have implications for understanding low latitude

15 climate phenomena such as El Niño-Southern Oscillation and monsoons in the past.

1   Introduction

Seasonality is one of the central characteristics of climate. It relates to the geometry of the Earth's orbit around the sun and the rotational axis configuration, and the effect of these on the amount and distribution of radiative energy received at the Earth's surface (Laepple and Lohmann, 2009; Milankovitch, 1941). The seasonality at a given latitude is largely determined

20 by the Earth-Sun distance and the angle at which sunlight reaches the Earth's surface, both defining the amount of radiative energy received seasonally and locally. Both parameters are influenced by variations in obliquity, eccentricity and precession (orbital longitude of the perihelion) that respectively describe the tilt of Earth rotational axis, the shape of the Earth orbit and the seasonal timing of Earth's closest proximity to the Sun. Seasonal cycles occur because the Earth's axis is tilted, with seasons having opposite timing in the two hemispheres. At low latitudes, where the surface inclination experiences limited

25 annual changes, the seasons are relatively mild. In some cases, such as on the Equator, seasonal variations in climate are barely noticeable except for changes in humidity. In the open ocean, the modern seasonal thermal contrast corresponding to

the annual amplitude of Sea Surface Temperature (SST) is in many tropical places much less than 2°C (e.g. Levitus, 1982; Harrison et al., 2009; Erb et al., 2015). The mean SST amplitude at the equator might have been different in the past during periods of high eccentricity (e = 0.05-0.06), owing to an annual variation of Earth-Sun distance of about 10-11% - compared

30   to 3.2 % under present day orbital configuration (e = 0.016) using the ellipse equation (Figure 1). At high eccentricity, Earth's more elliptical orbit indeed amplifies the effect of precession (Berger and Loutre, 1991). The latter alters the timing of the perihelion, with a periodicity of ca. 21 ka and determines the season of increased insolation. Elevated eccentricity amplifies the difference between the energy received at low latitudes at perihelion versus aphelion, inducing potential tropical seasonal fluctuations that impact meteorological factors. In particular, given the relation between SST and atmospheric dynamics, it

35   should also be expected that eccentricity shifts would affect wind-driven surface ocean circulation (Erb et al., 2015) and primary productivity (Beaufort et al., 2022). The impact of eccentricity-modulated precession variations has been extensively documented for various low latitude seasonal phenomena such as monsoons (e.g. Wang, 2009; Cheng et al., 2016; Prescott et al., 2019), ocean primary productivity (Beaufort et al., 1997; Le Mézo et al., 2017), African lake levels (Trauth et al., 2009), the Dole effect (low latitude vegetation and phytoplankton productivity)(Landais et al., 2010), and El Niño Southern Oscillation

40   (ENSO) (Clement et al., 1999; Timmermann et al., 2007; Ashkenazy et al., 2010; Erb et al., 2015), among others. Those studies generally focused on specific intervals, preventing a systematic understanding of the processes at play at the scale of one full orbital precession cycle as well as of the eccentricity dependence of the system response. Erb et al., (2015) demonstrated that high eccentricity-induced precession variations exert dual influences on the equatorial Pacific seasonal cycle. These effects manifest through direct thermodynamic alterations in insolation anomalies and consequential shifts in thermocline dynamics

45   driven by wind-stress responses to insolation changes. This research delved into the dependence of the modeled signal on eccentricity configuration. Furthermore, Chiang et al. (2022) revealed that the annual cycle in the Eastern Equatorial Pacific (Cold Tongue region) responds to an intricate effect of both the tilt of the Earth and Earth-Sun distance variation associated with eccentricity, with the eccentricity effect dominating over the obliquity one under highest eccentricity conditions. Beaufort et al., (2022) investigated the direct impact of Earth's orbital eccentricity on tropical surface ocean seasonality beyond the equatorial

50   Pacific. The cyclic diversification phases they observed in the evolution of coccolithophores spanning 2.8 million years closely follow the heightened seasonality during periods of high eccentricity. The distinctive eccentricity signature found in the records indeed differs from the one of the Pleistocene global climate cycles and ice volume variability, which rather follow high latitudes insolation forcing. While this study provided evidence of a significant seasonal pattern in surface conditions of the Indo-Pacific Ocean basins under high eccentricity, the simulation design utilizing only two precession configurations fell

55   short of capturing an entire precession cycle at high eccentricity, thus limiting a comprehensive analysis. Apart from the aforementioned investigations, only a limited number of modeling studies have addressed the combined sensitivity of SST and Primary Production (PP) dynamics at orbital time scales. These factors are nevertheless crucial in assessing paleoclimate dynamics, given the numerous proxy records associated with them. In the present study we use an Earth System Model that includes a marine biochemistry module to simulate SST and PP response to changes in precession at high eccentricity. Given

60   that the comprehension of the long-term seasonal dynamics within the tropical ocean (in particular that related to the seasonal timing of perihelion) requires a full precession cycle, we complemented simulations introduced by Beaufort et al. (2022) by

generating 4 additional runs at high eccentricity. With those, precession cycles are described by six different perihelion position at high eccentricity and two at low eccentricity. The setup we used aims at identifying direct ocean responses to changes in insolation, voluntarily excluding the potentially competing effects of ice-sheet extent, pCO2 and nutrient content variations.

65 With these results, we are able to show that when eccentricity was high, the low latitudes ocean experienced significant seasons related to a stronger annual change in the Earth-Sun distance.

2 Methods

2.1 Model and simulations setup

We used the IPSL-CM5A2 Earth System Model that integrates three key components: the LMDz5A atmospheric model (Hour-
70 din et al., 2013), the ORCHIDE (Krinner et al., 2005) land surface model, and the NEMOv3.6 oceanic model (Madec and The Nemo Team, 2015). The NEMO model encompasses the ocean dynamics component (OPA (Madec, 2008)), a sea-ice thermo-dynamics model (LIM2 (Fichefet and Maqueda, 1997)), and a biogeochemistry model (PISCES-v2 (Aumont et al., 2015)). The ocean grid has a horizontal resolution of 2° by 2° (refined to 0.5° in the tropics) and 31 vertical levels, with varying thickness from 10 m at the surface to 500 m at the ocean floor. The atmospheric grid has a horizontal resolution of 1.875° latitude by 3.75°
75 longitude and incorporates 39 vertical levels. The OASIS coupler (Valcke et al., 2012) facilitates the crucial ocean-atmosphere coupling by interpolating and exchanging variables between the two components. A detailed description of the IPSL-CM5A2 model and its performance in simulating pre-industrial climate can be found in Dufresne et al. (2013) and Sepulchre et al. (2020). The ocean biogeochemistry component of the model, PISCES-v2 (Aumont et al., 2015), simulates the primary oceanic biogeochemical cycles (C, P, Si, N, and Fe) and includes a simplified representation of lower trophic levels within the marine
80 ecosystem. It incorporates two phytoplankton size classes (nannophytoplankton and diatoms) and two zooplankton size classes (micro- and meso-zooplankton), along with five limiting nutrients (Fe, NO_3^-, NH_4^+, Si, and PO_4^{3-}). Phytoplankton growth is influenced by nutrient availability, light penetration, and water temperature. In the version of the model we used, river supply of all elements except DIC and alkalinity remains constant across simulations and is obtained from the GLOBAL-NEWS2 datasets (Mayorga et al., 2010). For further insights into the model parameterizations, see (Aumont et al., 2015). We conducted
85 eight equilibrium simulations, distinguished solely by their respective orbital parameters as shown in Table 1. Four of the simulations that we are using here have already been published (Beaufort et al., 2022; Beaufort et al., 2021). Out of the eight simulations, six were performed at high eccentricity, representing the most extreme values observed during the past million years. These high eccentricity simulations encompassed six distinct angles of precession in order to achieve a 60° resolution (2 months) of the perihelion motion in the orbital plane during a precession cycle. Additionally, two simulations were carried out
90 at the lowest eccentricity, where only two precession angles were considered due to the negligible impact of precession when eccentricity is low. Land-sea mask, ice-sheet configuration, as well as concentrations of CO_2 and other greenhouse gases were all set to pre-industrial values so we only focus on the direct effect of orbital configuration on the surface ocean. Each simulation was initiated from an equilibrated pre-industrial simulation conducted by Sepulchre et al. (2020) and was run for 500 additional model years. In the following, all variables are displayed as monthly averages over the final 100 years of each model

simulation and the net primary productivity is calculated by integrating values over the entire water column. We acknowledge that the duration of seasons is governed by the timing of perihelion, consequently influencing the length of each month in the Gregorian calendar (Joussaume and Braconnot, 1997). Nevertheless, in the context of this study, the impact remains limited, except for instances where monthly alignment to the calendar is presented: Hence in those figures showing the Gregorian calendar, for simplicity, the accuracy is scaled at a few days (its inherent precision). The description of the Earth's orbital system is from Berger and Loutre (1991) and Laskar (2020)and is illustrated in Figure 1. The timing of the orbital solution is from Laskar et al. (2004).

2.2 Comparison with modern conditions

For comparison with simulations, SST and PP datasets were used to illustrate their seasonality and annual average values. Modern SST data were gathered from the Comprehensive Ocean-Atmosphere Data Set (COADS), which compiles marine observations conducted by ships of opportunity between 1854 and 1992. These SSTs were edited and statistically summarized on a monthly basis for the period of 1961-1992, utilizing 2 degrees in latitude by 2 degrees in longitude cells (Slutz et al., 1985). Modern PP data estimates were acquired from MODIS satellite measurements taken between 1998 and 2021 (Slutz et al., 1985). This dataset provides monthly averaged measurements in grid cells of 7 km2. The data were averaged at a resolution of 1 degree in latitude by 1 degree in longitude, and subsequently, monthly averages were computed over the entire 1998-2021 period.

2.3 Seasonality analysis

In the following analysis we adopt the basic method of calculating the annual amplitude (e.g. Chen and Yu, 2015) of SST or PP by determining the difference between the highest and lowest monthly values for each grid point on the dataset, as in (Beaufort et al., 2022). We preferred this approach to seasonality indices commonly employed in the field of hydrology sciences to characterize the annual patterns of humidity or river flow - such as the duration of the rainy season, the seasonal ratio, or more intricate methods involving complex histograms (e.g. Laaha and Blöschl, 2006) - for its simplicity and robustness

2.4 Annual mean and amplitude analysis

We opt to average the six high eccentricity simulations when analyzing annual means and amplitudes owing to their congruence. We acknowledge the potential loss of certain interhemispheric dynamics present in seasonal variation of SST (Erb et al., 2015) through this averaging process, but the gain of clarity is substantial considering that such interhemispheric dynamics do not constitute the primary focus of this study. Given the near-identical patterns of SST and PP between the two low eccentricity simulations (R^2>0.99, N=79932), we also select only one of them (Ecc. min - P310) for comparison with the high eccentricity simulations. This choice is illustrated in Figure 2: when comparing the simulations with perihelion in December and in August at low (Fig. 2A for SST and 2B for PP) and high (Fig. 2C for SST and 2D for PP) eccentricities, the low eccentricity simulations

125 appeared largely better correlated than the high eccentricities simulations because precession has almost no effect at low eccentricity.

3 Results

3.1 Sea Surface Temperature dynamics

3.1.1 Annual Sea Surface Temperature

130 The simulated annual mean SST display consistency between the different simulations and with modern measurements (COADS) (Figure 3). These findings suggest that annual mean SST is minimally affected by eccentricity. This observation is consistent with expectations, as the variations in yearly radiative energy received by Earth as a result of eccentricity cycles are negligible (Imbrie et al., 1993 and Table 1).

3.1.2 Annual amplitude of SST

135 The examination of SST seasonality, as measured by the annual SST amplitude (Figure 3), reveals notable distinctions between different eccentricity states. In the present-day ocean and in the low eccentricity configuration, extensive ocean regions near the equator exhibit small seasonal amplitude (<2°C). In simulations with high eccentricity, only a small region in the western Pacific displays amplitudes lower than 2°C. The contrast in amplitude between high and low eccentricity simulations clearly indicates a substantial increase (at least 1°C) in seasonality across large part of the Indian, Atlantic, and eastern Pacific Oceans.

140 Few grid points (1.6%) show a lower amplitude under high eccentricity conditions compared to low eccentricity scenarios (Figure 4). The largest increase in seasonality with eccentricity occurs near the equator, (in average two time larger between 5°N and 5°S (1.2°C) compared to 0.6°C between both 30°N and 5°N and 5°S and 30°S).

3.1.3 Annual temperature cycles

In line with the previous paragraph, the analysis of the tropical seasonal cycle as depicted in Figure 5 reveals the absence of a
145 distinct annual SST cycle in both the modern data and the low eccentricity simulation (<0.5°C), whereas the high eccentricity simulations display annual amplitudes of approximately 2.2°C. Notably, the annual temperature cycle averaged over a wide latitude band (30°N-30°S) exhibits substantial variations dependent on precession conditions exclusively in the high eccentricity simulation, in contrast to the modern and low eccentricity cases. Similar outcomes were observed within a narrower latitude range (e.g., 5°N-5°S). The selection of this wide latitude range is intended to encompass tropical climate phenomena,
150 including the monsoon. Interestingly, the timing of the temperature peak differs among the high eccentricity simulations, indicating a progressive displacement of the warmest period in the year following the shift in the longitude of perihelion (ω) during a precession cycle. The warmest period typically occurs one to two months after perihelion, when the Earth reaches its closest distance to the sun, whereas the coldest period occurs approximately one to two months after aphelion, when the Earth is farthest from the sun. This establishes a direct connection between thermal seasons and precession, whereby the gradual but

155 significant warming of the ocean surface is attributed to the increased radiative energy received from the sun during perihelion. As expected, such a relationship between thermal seasons and precession is not observed in the two low eccentricity cases (present conditions and the low eccentricity simulation) ; despite their nearly opposite precession configurations ($\omega = 103°$ and $\omega = 310°$, respectively), both cases experience a relatively minor increase in temperature at the same period of the year (May).

3.2 Primary Productivity dynamics

160 #### 3.2.1 Annual primary production

The mean annual PP patterns exhibit strong similarity across all seven simulations and with the modern ocean (MODIS) (Figure 6). However, although the first order patterns of PP are similar, PP is under-estimated for the tropical Indian and Atlantic Oceans while overestimated in the Pacific equatorial upwelling, as discussed by Aumont et al. (2015). However those small discrepancies do not affect the present study that focuses on comparing high and low eccentricity simulations. Simulated

165 PP align with observations, revealing an equatorial band with higher productivity, and lower productivity zones located in the tropical gyres. This equatorial high annual PP area is the result of Ekman upwelling that bring nutrient-enriched water to the sub-surface (e.g., Mcclain and Firestone, 1993). In the Indian Ocean, the high PP areas spread northward in the Arabian Sea and Bay of Bengal due to the Ekman dynamics forced by the monsoon (Bauer et al., 1991). The similarity between the two maps (Figures 6B, and 6C) suggests that annual PP is minimally affected by eccentricity.

170 #### 3.2.2 Annual amplitude of Primary Production

The annual amplitude of PP exhibits heterogeneity and patchiness within the tropical band, as depicted in Figure 6. Areas characterized by seasonal upwelling, such as the monsoon zone, generally display the highest amplitudes, whereas oligotrophic regions exhibit lower amplitudes. Simulations with high eccentricity often yield higher amplitudes compared to those with low eccentricity (Figure 6). Approximately 70% of the area between 30°N and 30°S exhibit a positive difference, with an

175 average 11% increase in PP amplitude at high eccentricities (Figure 7A). The amplification of seasonal amplitude is particularly remarkable in the Indian Ocean and narrow equatorial bands of the western Pacific and Atlantic Oceans. The regions exhibiting the most pronounced PP amplitude differences between high and low eccentricities shift across the range of simulations. For instance, the Arabian sea upwelling zone demonstrates the highest amplitude difference in simulations with a longitude of perihelion (ω) of 87°, while the lowest difference is observed at $\omega = 315°$ (Figure 7B, C). In the latter simulation, the Indo-

180 Pacific Warm-Pool displays high seasonality at $\omega = 210°$, while much of the rest of the tropical oceans (equatorial Atlantic, eastern Pacific, and monsoon area) exhibit low seasonality (Figure 7D). The impact of eccentricity on the annual amplitude of PP is clearly illustrated in Figure 8, where the average PP and annual amplitude of PP between 30°N and 30°S are plotted for each simulation. The results reveal that the annual amplitude of PP significantly rises by up to 19% at low latitudes during periods of high eccentricity compared to low eccentricity, except when the longitude of the perihelion coincides with the March

185 equinox. In contrast, the increase in eccentricity does not seem to have a significant impact on mean annual PP, as indicated by

the minimal fluctuation (+/- 2%) observed in the simulated PP at high eccentricity, depending on for different longitude of the perihelion, compared to the simulated PP at low eccentricity (Figure 8A).

3.2.3 Annual Primary production cycles

Unlike SSTs in the tropics, which lack strong seasonality under low eccentricity conditions, tropical PP exhibit amplified sea-
190 sonality due to the annual wobbling of the Earth's axis. This seasonality is partly due to strongly seasonal phenomena such as monsoons and the seasonal migration of the Intertropical Convergence Zone (ITCZ). Based on seven simulations and modern observations, we observed that there are two seasons of decreased PP following the equinoxes. The highest tropical productivities occur two months after the solstices, as depicted in Figure 9. The annual cycle of PP remains relatively consistent across different precession states, but it is significantly amplified in simulations with high eccentricity. The impact of eccen-
195 tricity amplification can be examined by plotting PP in the precession time domain instead of the traditional annual time model (Figure 10). This representation reveals that the peak PP occurs when the perihelion aligns with a particular month or slightly earlier, and conversely at any given month, low PP lower occurs after the aphelion. It is important to note that each month in this figure is scaled differently, with the highest scale assigned to August because it is the month showing the highest PP in all simulations and modern data. Remarkably, the maximum productivity, reaching approximately 220 gC/m^2/year, coincides
200 with the perihelion occurring in August (ω=315°). This demonstrates that the regular shift of the perihelion during a precession cycle is intensified under high eccentricity conditions, similar to the impact observed on SST.

4   Discussion

4.1   Increased seasonality under high eccentricity

We show that the seasonality in the tropical ocean becomes more pronounced during periods of high eccentricity in Earth's
205 orbit. This effect is particularly evident in SSTs for which the seasonal cycle is muted in the present-day data and in the low eccentricity simulation, with an annual temperature amplitude of less than 0.5°C on average. In contrast, the high eccentricity simulations exhibit on average an annual thermal amplitude of 2.2°C, highlighting the significant increase in seasonal variabil-ity. This result is in agreement with Ashkenazy et al. (2010) who simulated equatorial (4°N-4°S) oceans at high eccentricity with the autumn and spring equinoctial precessions (201,000 and 213,000 years ago) and found large SST seasonal cycles
210 of about 2°C in the three oceanic basins with very little mean annual temperature change. Erb et al. (2015) further examined the impact of eccentricity modulated precession configurations on zonal wind anomalies associated with changes in subtropi-cal anticyclone strength and their influence on shifts in convection regions in the western equatorial Pacific. They found that "changes in annual-mean SST in the tropics are generally relatively small" (Erb et al., 2015; P.9263) but did not further ex-pand on this observation. The annual amplitude Pacific SST however increases by 2°C in their idealized high eccentricity
215 simulations (e = 0.049) compared to the preindustrial one (e= 0.0167, ω=103°), aligning closely with our own experimental results as well. Consequently, we assert with confidence that higher eccentricity values would lead to a seasonal SST increase

of approximately 2°C, as substantiated by consistent findings from different sensitivity experiments using different numerical models. To visualize the impact of eccentricity and precession effect on SST in the time domain, we compute an estimate of a transient signal over a 900,000-year period. This is based on a linear eccentricity scaling of the six precession simulations placed in a chronologic framework for which precession and eccentricity values are known (Laskar et al., 2004), with the following equation: $Yt = (HE_\omega - LE).e_t/0.053$ Here, Yt represents the SST or PP value of annual average or amplitude at time t, HEω denotes the simulated value for a given perihelion longitude (ω) under high eccentricity, LE signifies the simulated value under low eccentricity (ω= 315°), et represents the eccentricity at time t, and 0.053 corresponds to the eccentricity value used for the high eccentricity simulation. Figure 11 illustrates that while the mean annual SST signal in the tropics remains unaffected by eccentricity, the seasonal amplitude experiences a significant increase at eccentricity frequencies (ca. 100 ka and 400 ka) with no real effect of precession cycles. On the other hand, annual mean PP displays greater sensitivity to precession than SST, while its response to eccentricity seems to be relatively minimal. Eccentricity does however significantly affect PP seasonality, except when the perihelion aligns closely with the vernal equinox. Unlike SST, PP exhibits inherent seasonality in the modern low latitude oceans. For instance, in the Indian monsoon region, PP reaches its peak during summer and declines at the solstices (e.g. Longhurst, 1995). The PP phenology remains stable without following the path of precession. This is because seasonal dynamics of productivity in those regions is strongly tied to the oceanic circulation associated with ITCZ that crosses the equator twice a year during solstices (e.g. Longhurst, 1995; Pennington et al., 2006). This occurs because wind-driven open ocean upwelling (e.g. Mann and Lazier, 1996) reaches a maximum when the ITCZ has seasonally migrated farthest from the equator, aligning with the peak of the summer seasons in both hemispheres (Longhurst, 1995): the winds are minimal at the atmospheric convergence zones, including the ITCZ (Pennington et al., 2006). When eccentricity is high, this phenomenon is enhanced, preserving its seasonality. Consequently, when the perihelion aligns with the equinox, PP annual mean also reaches its lowest values regardless of eccentricity levels. This explains why, in Figure 11, PP seasonality exhibits significant precession variability, in contrast to SST.

4.2 Gradual Drift of Seasons within the Calendar Year

Figure 4 reveals that the evolution of SSTs is influenced by the annual positioning of perihelion and aphelion, with a lag of a few months. Clement et al. (1999) used a simplified ocean-atmosphere model to investigate the influence of precession cycles spanning 150,000 years on El Niño-Southern Oscillation (ENSO). They noted shifts in seasonal energy distribution across the tropical Pacific Ocean, with the strength and frequency of El Niño events impacted by the interplay of precession and eccentricity-driven changes in energy excess timing and location. This is coherent with Erb et al. (2015), who observed a delayed seasonal shift in Equatorial Pacific SST maxima following perihelion movement in precession simulations, attributed partly to direct insolation forcing. Furthermore, Chiang et al. (2022) demonstrated the Earth-Sun distance's role, resulting from precession and eccentricity coupling, in bolstering equatorial Pacific wind patterns pivotal to the Walker circulation. In our study, the six simulations we performed at high eccentricity allowed us to observe a complete revolution of precession at a 2-month resolution (Figure 12), highlighting a gradual shift of seasons. The seasonality pattern described here differs from the familiar seasons we experience at mid latitudes, where summers and winters are defined to start at the solstices. Our results

rather suggest that in low latitudes and at high eccentricity, the warm season does not begin at the same calendar date each year; rather, it progresses along the Earth's orbit and calendar at a rate of approximately 0.017° per year (25 minutes), equivalent to a cycle of approximately 21,000 years. This advancement occurs due to the shifting moment when the Earth approaches its closest point to the sun (perihelion), attributed to the precession of the equinoxes. While the common extra-tropical seasons

255 are fixed in our calendars, those 'tropical seasons' are therefore not subject to fixed calendar dates and follow this progressive shift in time due to changing precession. We investigated whether the 'tropical seasons,' as described earlier, exert an influence on PP, which typically follows also a 'classical' seasonal cycle and the migration of the ITCZ, dictated by the tilt of the Earth's axis. Figure 13 illustrates the monthly average PP values for the 30°N-30°S oceans in the low eccentricity simulations, subtracted from the PP values simulated in each precession configuration at high eccentricity for the corresponding month. The

260 plotted results mirror those in Figure 12, demonstrating a shift in PP similar to SST but with a reduced delay from perihelion. These findings emphasize the significance of the 'tropical seasons' on PP dynamics. The seasonal variation in radiative energy at high eccentricity leads to a direct forcing on PP, as evidenced by its observed seasonality.

4.3 Eccentriseasons

Due to the distinct origin of the seasonal variations that we have illustrated in this study, arising from the Earth's orbital

265 eccentricity rather than the tilt of its rotation axis, we suggest that a distinct and appropriate nomenclature is needed. We propose the term 'eccentriseason', derived from a clipped compound of 'eccentricity' and 'season'. Eccentriseasons are defined as seasons occurring at low latitude in response to the cycles of the Earth-Sun distance: their annual amplitude increases with eccentricity, and their timing gradually shift of about 25 minutes per year on the calendar in accordance with the precession of the equinoxes (see Figure 1). Eccentriseasons are therefore distinct from the familiar extra-tropical seasons which remains

270 stable in the calendar and are less dependent on eccentricity.

4.4 Implications of eccentriseasons on paleoclimatology

The increase in seasonality within the tropical ocean would significantly affects low latitude climate phenomena: The rise in tropical sea surface temperature during key seasons has a notable impact on energy transfer, influencing monsoons, migration of the Intertropical Convergence Zone, and ENSO dynamics. The relationships between these phenomena and the amplified

275 seasonality are intricate and have already been explored in dedicated studies (Clement et al., 1999; Timmermann et al., 2007; Braconnot et al., 2008; Ashkenazy et al., 2010; Erb et al., 2015; Chiang et al., 2022). This study does not focus on exploring these mechanisms.

The ocean's ecology, particularly that of phytoplankton, represents the cumulative outcome of localized climatic mechanisms. A study exploring phytoplankton's biological evolution has delineated the ecological impacts of eccentriseasons on

280 marine phytoplankton (Beaufort et al., 2022): Over the past 2.8 million years, the evolution of coccolithophores has been observed to directly align with the eccentricity cycles, displaying minimal influence from global climates. This pattern is interpreted as a result of cyclic diversification in low latitude ecological niches during periods of heightened tropical seasonality in high eccentricity times. The present work highlights significant sea surface temperature (SST) seasonality, which likely plays

a crucial role in the mechanisms (e.g. wind patterns, ocean circulation intensity, biologic productivity, biologic evolution) described in Beaufort et al. (2022).

The lack of a significant precession effect on low latitude mean annual primary production in our simulations is surprising, given that many paleoproductivity records show a strong response to precession (e.g. Molfino and Mcintyre, 1990; Beaufort et al., 1997; Villanueva et al., 2001; Moreno et al., 2002; Su et al., 2015; Deik et al., 2017; Tangunan et al., 2017). Past PP reconstructions for coccolithophores rely on annual reconstructions of primary production (Beaufort et al., 1997; Hernández-Almeida et al., 2019). However, modern data for primary production suggest that a linear relationship exist between mean annual PP and the annual amplitude of PP variations, with the latter being approximately half of annual PP (Figure 13). By converting the annual PP results into amplitude PP (or seasonality) records using a scaling factor of 0.59 (adjusted for the Indian Ocean, Figure 14), a comparison with simulated seasonal PP for a specific region (72-77°E, 3-7°N), where the core used in Beaufort et al. (1997) is located, reveals striking similarities (Figure 15). This suggest the significance of seasonality as an important parameter that may have been overlooked when studying paleoproductivity in low latitudes.

Alkenones and Mg/Ca are two proxies for SST that are commonly used in paleoceanography (e.g. Brassell et al., 1986; Prahl et al., 1988; Rosell-Melé et al., 1995; Sonzogni et al., 1997; Rosenthal et al., 2000). The alkenones production presents a seasonality dependent on the coccolithophores (Emiliania huxleyi) phenology (Rosell-Melé et al., 1995; Sikes et al., 1997; Ternois et al., 1998). Similarly, planktonic foraminifera, produce tests from which Mg/Ca SST estimates at specific seasons (e.g. Fairbanks et al., 1982; Mohtadi et al., 2009; Chaabane et al., 2023). The production seasons of these organisms has been used to explain differences in Holocene SST reconstructions from the same site using different proxies having different phenologies (Leduc et al., 2010; Lohmann et al., 2013; Bova et al., 2021). Our results suggest regular phenological phase shifts between primary production and sea surface temperature eccentriseasons. Crucially, our results suggest that regular phenological phase shifts occur between primary production and sea surface temperature eccentriseasons. For example, a plankton population always displaying peak production during the September high-productivity season would experience, throughout a precession cycle, a larger SST signal (typically with an amplitude of 2.5°C) than an organism that prospers year-round and is thus insensitive to the shift in the month of maximum SST related to eccentriseasons (Fig 4). Therefore, it is imperative to account for the alignment between proxy producers' phenology and temperature fluctuations across the calendar year driven by eccentriseasons, ensuring accurate interpretations of SST records and mitigating seasonal biases. In line with our proposition, proxies accurately estimating mean annual SST (i.e., growing throughout the year) are expected to exhibit less precession-band variance that those with a seasonal growth pattern, which should record a precession component (Fig. 11).

An additional illustration of the impact of changes in annual SST amplitude can be observed in the evolution of phytoplankton in tropical regions, which responds notably to heightened seasonality during periods of high eccentricity, as discussed in Beaufort et al. (2022). The morphologic evolution records presented in this work appeared to respond more to eccentricity than precession. This suggests that temperature plays a pivotal role in delineating distinct seasonal niches, thereby promoting diversification into new species among isolated phytoplankton populations.

5 Conclusions

In this study, we investigated the response of low-latitude surface oceans to variations in Earth's orbital eccentricity using the Earth System Model IPSL-CM5A2 including its marine biogeochemistry module PISCES-v2. Our climate simulations
320 reveal that high eccentricity leads to increased seasonality in SST in low-latitude ocean surface waters, with an annual thermal amplitude of 2.2°C on average. In contrast, PP that already exhibits inherent seasonality under low eccentricity conditions, sees its seasonal cycle significantly enhanced under high eccentricity conditions. The consequences of this amplification of seasonality under high eccentricity configuration are significant: on long time scales, this results in SST seasonality following only eccentricity frequencies, while PP seasonality follows both eccentricity and precession frequencies. The positioning of
325 perihelion during the year directly affects the SST and PP seasonalities under high eccentricity, leading to a gradual shift of seasons within the calendar year. To account for this phenomenon, we introduce the term "eccentriseasons" that describes these distinct annual thermal differences observed in tropical oceans under high eccentricity conditions, which shift gradually throughout the calendar year. This study contributes to the growing body of knowledge about the role of orbital parameters in shaping Earth's climate over long time scales and highlights the significance of eccentricity-induced seasonality in low-latitude
330 regions. Our results may have important implications for understanding low-latitude climatic phenomena that have a strongly seasonal nature, such as ENSO and monsoons. The increased seasonality in tropical oceans under high eccentricity conditions can for example influence energy transfer and ocean dynamics which in turn affect those climate phenomena in the past. Our results also have potential implications for paleoclimatology studies: we highlight here the significance of seasonality as a parameter that may have been overlooked when studying paleoproductivity in low latitudes. This insight can inform
335 the interpretation of paleoproductivity records and proxies commonly used in tropical paleoceanography, because our study suggests that the interactions between seasonal production and shifting temperature seasonality likely imprints the signal that is recorded.

Code availability. Code availability LMDZ, XIOS, NEMO, and ORCHIDEE are released under the terms of the CeCILL license. OASIS-MCT is released under the terms of the Lesser GNU General Public License (LGPL). Up to date IPSL-CM5A2 source code is pub-
340 licly available through svn, with the following commands line: svn co http://forge.ipsl.jussieu.fr/igcmg/svn/modipsl/branches/publications/ IPSLCM5A2.1_11192019modipsl;cdmodipsl/util;./modelIPSLCM5A2.1 information regarding the different revisions used, namely:

- NEMOGCM branch `nemo_v3_6_STABLE` revision 6665
- XIOS2 branch `branches/xios-2.5` revision 1763
- IOIPSL/src svn `tags/v2_2_2`
345 - LMDZ5 branch `branches/IPSLCM5A2.1` rev 3591
- `branches/publications/ORCHIDEE_IPSLCM5A2.1.r5307` rev 6336
- OASIS3-MCT 2.0_branch (rev 4775 IPSL server)

The login/password combination requested at first use to download the ORCHIDEE component is anonymous/anonymous. We recommend that you refer to the project website: http://forge.ipsl.jussieu.fr/igcmg_doc/wiki/Doc/Config/IPSLCM5A2 for a proper installation and

350 compilation of the environment. In addition, source code of the version used for this paper is publicly available at https://doi.org/10.5281/zenodo.6772699 (Pillot, 2022).

Data availability. The model outputs are archived at the SEANOE data repository : https://www.seanoe.org/data/00728/84031/ for the outputs published in Beaufort et al., (2022) and https://www.seanoe.org/data/xxxx/xxxxx/ for the new model ouputs

Author contributions. LB and ACS designed the experimental approach. ACS performed the simulations. LB analyzed the results and prepare

355 the figures. Both authors wrote the manuscript

Competing interests. LB is an editor at Climate of the Past

Acknowledgements. We thank Anthony Gramoullé for the help extracting relevant information from model outputs. We thank Christophe Menkes for helpful discussions, and Clara Bolton for reading an early version of the manuscript. Luc Beaufort is supported by the Agence Nationale de la Recherche (ANR22 ESDIR 003-ITCH). Anta-C. Sarr is supported by a grant from Labex OSUG (Investissements d'avenir

360 – ANR10 LABX56). Anta-C. Sarr was granted access to HPC resources of TGCC under allocation 2022-A0090102212 made by GENCI. Colored figures in this paper were made with perceptually uniform, color-vision-deficiency-friendly scientific color maps (Crameri et al., 2020), developed and distributed by Fabio Crameri (https://www.fabiocrameri.ch/colourmaps/).

References

Ashkenazy, Y., Eisenman, I., Gildor, H., and Tziperman, E.: The Effect of Milankovitch Variations in Insolation on Equatorial Seasonality, Journal of Climate, 23, 6133–6142, https://doi.org/10.1175/2010JCLI3700.1, 2010.

Aumont, O., Éthé, C., Tagliabue, A., Bopp, L., and Gehlen, M.: PISCES-v2: an ocean biogeochemical model for carbon and ecosystem studies, Geoscientific Model Development Discussions, 8, 1375–1509, 2015.

Bauer, S., Hitchcock, G. L., and Olson, D. B.: Influence of monsoonally-forced Ekman dynamics upon surface layer depth and plankton biomass distribution in the Arabian Sea, Deep-Sea Research, Part A (Oceanographic Research Papers), 38, 531–531–53, https://search.ebscohost.com/login.aspx?direct=true&db=inh&AN=3938699&site=eds-live, 1991.

Beaufort, L., Lancelot, Y., Camberlin, P., Cayre, O., Vincent, E., Bassinot, F., and Labeyrie, L.: Insolation cycles as a major control of the Equatorial Indian Ocean primary production, Science, 278, 1451–1454, 1997.

Beaufort, L., Bolton, C. T., and Sarr, A. C.: Morphometry, and mass accumulation rates of Indo-Pacific Pleistocene coccoliths and associated Climatic Simulations, https://doi.org/10.17882/84031, section: 2021-10, 2021.

Beaufort, L., Bolton, C. T., Sarr, A. C., Suchéras-Marx, B., Rosenthal, Y., Donnadieu, Y., Barbarin, N., Bova, S., Cornuault, P., Gally, Y., Gray, E., Mazur, J. C., and Tetard, M.: Cyclic evolution of phytoplankton forced by changes in tropical seasonality, Nature, 601, 79–84, https://doi.org/10.1038/s41586-021-04195-7, edition: 2021/12/03, 2022.

Berger, A. and Loutre, M. F.: Insolation values for the climate of the last 10 Million years, Quaternary Science Reviews, 10, 297–317, 1991.

Berger, A., Loutre, M.-F., and Tricot, C.: Insolation and Earth's orbital periods, Journal of Geophysical Research: Atmospheres, 98, 10 341–10 362, https://doi.org/10.1029/93JD00222, 1993.

Bova, S., Rosenthal, Y., Liu, Z., Godad, S. P., and Yan, M.: Seasonal origin of the thermal maxima at the Holocene and the last interglacial, Nature, 589, 548–553, https://doi.org/10.1038/s41586-020-03155-x, 2021.

Braconnot, P., Marzin, C., Gregoire, L., Mosquet, E., and Marti, O.: Monsoon response to changes in Earth's orbital parameters: comparisons between simulations of the Eemian and of the Holocene, Clim. Past., 4, 281–294, ://000262410700007, 2008.

Brassell, S., Brereton, R., Eglinton, G., Grimalt, J., Liebezeit, G., Marlwe, I., Pflaumann, U., and Sarnthein, M.: Paleoclimatic signals recognized by chemomtric treatment of molecular stratigraphic data, Orgaanic Geochemistry, 10, 649–660, 1986.

Chaabane, S., de Garidel-Thoron, T., Giraud, X., Schiebel, R., Beaugrand, G., Brummer, G.-J., Casajus, N., Greco, M., Grigoratou, M., Howa, H., Jonkers, L., Kucera, M., Kuroyanagi, A., Meilland, J., Monteiro, F., Mortyn, G., Almogi-Labin, A., Asahi, H., Avnaim-Katav, S., Bassinot, F., Davis, C. V., Field, D. B., Hernández-Almeida, I., Herut, B., Hosie, G., Howard, W., Jentzen, A., Johns, D. G., Keigwin, L., Kitchener, J., Kohfeld, K. E., Lessa, D. V. O., Manno, C., Marchant, M., Ofstad, S., Ortiz, J. D., Post, A., Rigual-Hernandez, A., Rillo, M. C., Robinson, K., Sagawa, T., Sierro, F., Takahashi, K. T., Torfstein, A., Venancio, I., Yamasaki, M., and Ziveri, P.: The FORCIS database: A global census of planktonic Foraminifera from ocean waters, Scientific Data, 10, 354, https://doi.org/10.1038/s41597-023-02264-2, 2023.

Chen, G. and Yu, F.: An objective algorithm for estimating maximum oceanic mixed layer depth using seasonality indices derived from Argo temperature/salinity profiles, Journal of Geophysical Research: Oceans, 120, 582–595, https://doi.org/10.1002/2014JC010383, 2015.

Cheng, H., Edwards, R. L., Sinha, A., Spötl, C., Yi, L., Chen, S., Kelly, M., Kathayat, G., Wang, X., Li, X., Kong, X., Wang, Y., Ning, Y., and Zhang, H.: The Asian monsoon over the past 640,000 years and ice age terminations, Nature, 534, 640, https://doi.org/10.1038/nature18591, 2016.

Chiang, J. C. H., Atwood, A. R., Vimont, D. J., Nicknish, P. A., Roberts, W. H. G., Tabor, C. R., and Broccoli, A. J.: Two annual cycles of
400   the Pacific cold tongue under orbital precession, Nature, 611, 295–300, https://doi.org/10.1038/s41586-022-05240-9, 2022.

Clement, A., Seager, R., and Cane, M.: Orbital controls on the El Nino/Southern Oscillation and the tropical climate, Paleoceanography,
        14, 441–456, 1999.

Deik, H., Reuning, L., and Pfeiffer, M.: Orbital scale variation of primary productivity in the central equatorial Indian Ocean (Maldives)
        during the early Pliocene, Palaeogeography, Palaeoclimatology, Palaeoecology, 480, 33–41, https://doi.org/10.1016/j.palaeo.2017.05.012,
405   2017.

Dufresne, J.-L., Foujols, M.-A., Denvil, S., Caubel, A., Marti, O., Aumont, O., Balkanski, Y., Bekki, S., Bellenger, H., and Benshila, R.:
        Climate change projections using the IPSL-CM5 Earth System Model: from CMIP3 to CMIP5, Climate dynamics, 40, 2123–2165, 2013.

Erb, M. P., Broccoli, A. J., Graham, N. T., Clement, A. C., Wittenberg, A. T., and Vecchi, G. A.: Response of the Equatorial Pacific Seasonal
        Cycle to Orbital Forcing, Journal of Climate, 28, 9258–9276, https://doi.org/10.1175/JCLI-D-15-0242.1, 2015.

410 Fairbanks, R. G., Sverdlove, M., Free, R., Wiebe, P. H., and Bé, A. W. H.: Vertical distribution and isotopic fractionation of living planktonic
        foraminifera from the Panama Basin, Nature, 298, 841–844, https://doi.org/10.1038/298841a0, 1982.

Fichefet, T. and Maqueda, M. M.: Sensitivity of a global sea ice model to the treatment of ice thermodynamics and dynamics, Journal of
        Geophysical Research: Oceans, 102, 12 609–12 646, 1997.

Harrison, D., Chiodi, A., and Vecchi, G.: Effects of surface forcing on the seasonal cycle of the eastern equatorial Pacific, Journal of Marine
415   Research, 67, 701–729, 2009.

Hernández-Almeida, I., Ausín, B., Saavedra-Pellitero, M., Baumann, K. H., and Stoll, H. M.: Quantitative reconstruction of primary pro-
        ductivity in low latitudes during the last glacial maximum and the mid-to-late Holocene from a global Florisphaera profunda calibration
        dataset, Quaternary Science Reviews, 205, 166–181, https://doi.org/10.1016/j.quascirev.2018.12.016, 2019.

Hourdin, F., Foujols, M.-A., Codron, F., Guemas, V., Dufresne, J.-L., Bony, S., Denvil, S., Guez, L., Lott, F., and Ghattas, J.: Impact of
420   the LMDZ atmospheric grid configuration on the climate and sensitivity of the IPSL-CM5A coupled model, Climate Dynamics, 40,
        2167–2192, 2013.

Imbrie, I., Berger, A., Boyle, E., Clemens, S., Duffy, A., Howard, W., Kukla, G., Kutzbach, J., Martinson, D., McIntyre, A., Mix, A.,
        Molfino, B., Morley, J., Peterson, L., Pisias, N., Prell, W., Raymo, M., Shackleton, N., and Toggweier, J.: On the structure and origin of
        major Glaciation cycles2. the 100,000-year cycle, Paleoceanography, 8, 699–736, 1993.

425 Joussaume, S. and Braconnot, P.: Sensitivity of paleoclimate simulation results to season definitions, Journal of Geophysical Research:
        Atmospheres, 102, 1943–1956, 1997.

Krinner, G., Ciais, P., Viovy, N., and Friedlingstein, P.: A simple parameterization of nitrogen limitation on primary productivity for global
        vegetation models, Biogeosciences Discussions, 2, 1243–1282, 2005.

Laaha, G. and Blöschl, G.: Seasonality indices for regionalizing low flows, Hydrological Processes: An International Journal, 20, 3851–3878,
430   2006.

Laepple, T. and Lohmann, G.: Seasonal cycle as template for climate variability on astronomical timescales, Paleoceanography, 24,
        https://doi.org/10.1029/2008PA001674, 2009.

Landais, A., Dreyfus, G., Capron, E., Masson-Delmotte, V., Sanchez-Goñi, M. F., Desprat, S., Hoffmann, G., Jouzel, J., Leuenberger,
        M., and Johnsen, S.: What drives the millennial and orbital variations of δ18Oatm?, Quaternary Science Reviews, 29, 235–246,
435   https://doi.org/10.1016/j.quascirev.2009.07.005, 2010.

Laskar, J.: Chapter 4 - Astrochronology, in: Geologic Time Scale 2020, pp. 139–158, Elsevier, https://doi.org/10.1016/B978-0-12-824360-2.00004-8, 2020.

Laskar, J., Robutel, P., Joutel, F., Gastineau, M., Correia, A. C. M., and Levrard, B.: A long-term numerical solution for the insolation quantities of the Earth, Astronomy & Astrophysics, 428, 261–285, https://doi.org/10.1051/0004-6361:20041335, 2004.

440 Le Mézo, P., Beaufort, L., Bopp, L., Braconnot, P., and Kageyama, M.: From monsoon to marine productivity in the Arabian Sea: insights from glacial and interglacial climates, Climate of the Past, 13, 759, 2017.

Leduc, G., Schneider, R., Kim, J. H., and Lohmann, G.: Holocene and Eemian sea surface temperature trends as revealed by alkenone and Mg/Ca paleothermometry, Quaternary Science Reviews, 29, 989–1004, https://doi.org/10.1016/j.quascirev.2010.01.004, 2010.

Levitus, S.: Climatological Atlas of the World Ocean, vol. 13 of *Professional Paper*, NOAA, 1982.

445 Lohmann, G., Pfeiffer, M., Laepple, T., Leduc, G., and Kim, J. H.: A model-data comparison of the Holocene global sea surface temperature evolution, Clim. Past, 9, 1807–1839, https://doi.org/10.5194/cp-9-1807-2013, 2013.

Longhurst, A.: Seasonal cycles of pelagic production and consumption, Prog. Oceanog., 36, 77–167, 1995.

Madec, G.: NEMO reference manual, ocean dynamics component: NEMO-OPA, Preliminary version. Note du Pole de modélisation, Institut Pierre-Simon Laplace (IPSL), France, 27, 1288–161, 2008.

450 Madec, G. and the NEMO team: NEMO reference manual 3_6_STABLE: NEMO ocean engine, Note du Pôle de modélisation, Institut Pierre-Simon Laplace (IPSL), France, 2015.

Mann, K. and Lazier, J.: Dynamics of Marine Ecosystems, Blackwell Sciences, Oxford, 1996.

Mayorga, E., Seitzinger, S. P., Harrison, J. A., Dumont, E., Beusen, A. H., Bouwman, A., Fekete, B. M., Kroeze, C., and Van Drecht, G.: Global nutrient export from WaterSheds 2 (NEWS 2): model development and implementation, Environmental Modelling & Software,

455   25, 837–853, 2010.

McClain, C. R. and Firestone, J.: An investigation of Ekman upwelling in the North Atlantic, Journal of Geophysical Research: Oceans, 98, 12 327–12 339, 1993.

Milankovitch, M.: Canon of insolation and the ice-age problem, Beograd: Koniglich Serbische Akademie. [English trans. Israel Prog. Sc. Translations, pub. US Dept. Com. and NSF, 1969], 1941.

460 Mohtadi, M., Steinke, S., Groeneveld, J., Fink, H. G., Rixen, T., Hebbeln, D., Donner, B., and Herunadi, B.: Low-latitude control on seasonal and interannual changes in planktonic foraminiferal flux and shell geochemistry off south Java: A sediment trap study, Paleoceanography, 24, https://doi.org/10.1029/2008PA001636, 2009.

Molfino, B. and McIntyre, A.: Precessional forcing of the nutricline dynamics in the Equatorial Atlantic, Science, 249, 766–769, 1990.

Moreno, A., Nave, S., Kuhlmann, H., Canals, M., Targarona, J., Freudenthal, T., and Abrantes, F.: Productivity response in the North Ca-

465   nary Basin to climate changes during the last 250 000 yr: a multi-proxy approach, Earth and Planetary Science Letters, 196, 147–159, https://doi.org/10.1016/S0012-821X(01)00605-7, 2002.

Pennington, J. T., Mahoney, K. L., Kuwahara, V. S., Kolber, D. D., Calienes, R., and Chavez, F. P.: Primary production in the eastern tropical Pacific: A review, Progress in Oceanography, 69, 285–317, https://doi.org/10.1016/j.pocean.2006.03.012, 2006.

Prahl, F. G., Muehlhausen, L. A., and Zahnle, D. L.: FURTHER EVALUATION OF LONG-CHAIN ALKENONES AS INDICA-

470   TORS OF PALEOCEANOGRAPHIC CONDITIONS, Geochimica Et Cosmochimica Acta, 52, 2303–2310, https://doi.org/10.1016/0016-7037(88)90132-9, 1988.

Prescott, C. L., Haywood, A. M., Dolan, A. M., Hunter, S. J., and Tindall, J. C.: Indian monsoon variability in response to orbital forcing during the late Pliocene, Global and Planetary Change, 173, 33–46, https://doi.org/10.1016/j.gloplacha.2018.12.002, 2019.

Rosell-Melé, A., Eglinton, G., Pflaumann, U., and Sarnthein, M.: Atlantic core-top calibration of the U37K index as a sea-surface palaeotem-
475   perature indicator, Geochimica et Cosmochimica Acta, 59, 3099–3107, https://doi.org/10.1016/0016-7037(95)00199-A, 1995.

Rosenthal, Y., Lohmann, G. P., Lohmann, K. C., and Sherrell, R. M.: Incorporation and preservation of Mg in Globigerinoides sacculifer:
       Implications for reconstructing the temperature and 18O/16O of seawater, Paleoceanogr., 15, 135–145, 2000.

Sepulchre, P., Caubel, A., Ladant, J.-B., Bopp, L., Boucher, O., Braconnot, P., Brockmann, P., Cozic, A., Donnadieu, Y., and Dufresne,
       J.-L.: IPSL-CM5A2–an Earth system model designed for multi-millennial climate simulations, Geoscientific Model Development, 13,
480   3011–3053, 2020.

Sikes, E. L., Volkman, J. K., Robertson, L. G., and Pichon, J.-J.: Alkenones and alkenes in surface waters and sediments of the
       Southern Ocean: Implications for paleotemperature estimation in polar regions, Geochimica et Cosmochimica Acta, 61, 1495–1505,
       https://doi.org/10.1016/S0016-7037(97)00017-3, 1997.

Slutz, R., Lubker, S., Hiscox, J., Woodruff, S., Jenne, R., Steurer, P., and Elms, J.: Comprehensive Ocean-Atmosphere Data Set; Release 1,
485   1985.

Su, X., Liu, C., Beaufort, L., Barbarin, N., and Jian, Z.: Differences in late quaternary primary productivity between the western tropical
       pacific and the south China sea: Evidence from coccoliths, Deep Sea Research Part II: Topical Studies in Oceanography, 2015.

Tangunan, D., Baumann, K.-H., Pätzold, J., Henrich, R., Kucera, M., De Pol-Holz, R., and Groeneveld, J.: Insolation forcing of coccol-
       ithophore productivity in the western tropical Indian Ocean over the last two glacial-interglacial cycles, Paleoceanography, 32, 692–709,
490   https://doi.org/10.1002/2017PA003102, 2017.

Ternois, Y., Sicre, M.-A., Boireau, A., L., B., and Jeandel, C.: Hydrocarbon, sterols, and alkenones insinking partilces of the Southern Ocean,,
       Organic Geochemistry, 1998.

Timmermann, A., Lorenz, S. J., An, S.-I., Clement, A., and Xie, S.-P.: The Effect of Orbital Forcing on the Mean Climate and Variability of
       the Tropical Pacific, Journal of Climate, 20, 4147–4159, https://doi.org/10.1175/JCLI4240.1, 2007.

495   Trauth, M. H., Larrasoaña, J. C., and Mudelsee, M.: Trends, rhythms and events in Plio-Pleistocene African climate, Quaternary science
       reviews, 28, 399–411, 2009.

Valcke, S., Balaji, V., Craig, A., DeLuca, C., Dunlap, R., Ford, R., Jacob, R., Larson, J., O'Kuinghttons, R., and Riley, G.: Coupling tech-
       nologies for earth system modelling, Geoscientific Model Development, 5, 1589–1596, 2012.

Villanueva, J., Calvo, E., Pelejero, C., Grimalt, J. O., Boelaert, A., and Labeyrie, L.: A latitudinal productivity band in the central North
500   Atlantic over the last 270 kyr: An alkenone perspective, Paleoceanography, 16, 617–626, https://doi.org/10.1029/2000PA000543, 2001.

Wang, P. X.: Global monsoon in a geological perspective, Chin. Sci. Bull., 54, 1113–1136, https://doi.org/10.1007/s11434-009-0169-4, 2009.
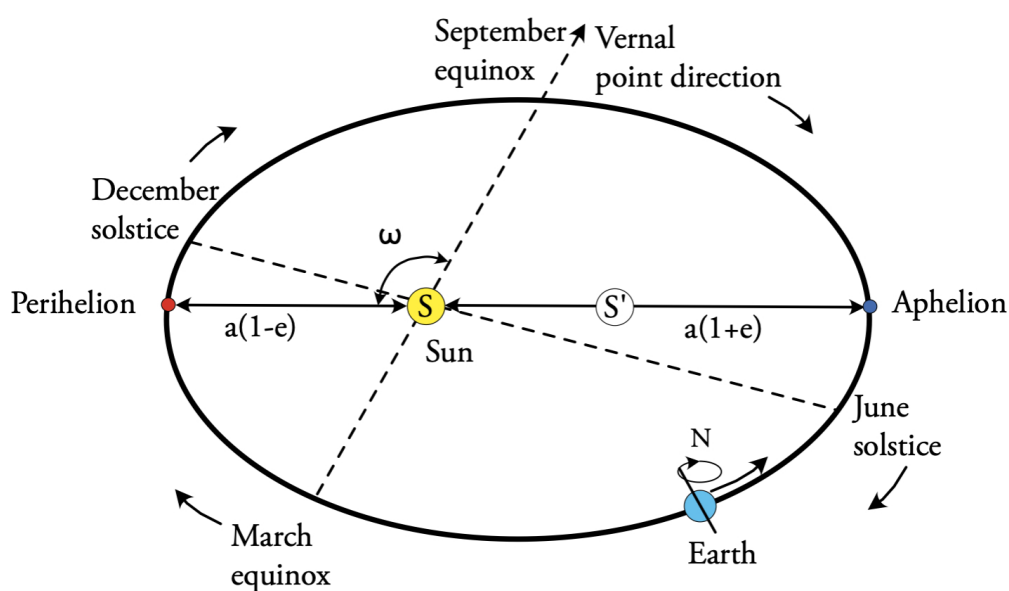
Figure 1. Schematic Illustration of Earth's Orbit Eccentricity and Precession (adapted from Berger et al., 1993 and Laskar, 2020): The Sun (S) occupies one focus of the elliptical Earth orbit, which is traced counterclockwise. The eccentricity (e) signifies the ratio of the distance between the foci (S and S') to the major axis's length (2a). During perihelion, when Earth is nearest the Sun, the Earth-Sun distance equates to a(1-e). At aphelion, Earth's farthest point from the Sun, the distance becomes a(1+e). The annual Earth-Sun distance variation, in percentage, equals the eccentricity multiplied by 200. The perihelion longitude (ω) denotes the angle between the Vernal Point direction (this direction is that of the sun observed during the march equinox) and the perihelion directions. Precession causes a gradual clockwise shift of the Vernal equinox (25 minutes per year, or 60 minutes x 24 hours x 365 days / 21,000 years). The equinoxes and solstices are represented close to their modern positions where Earth is at the perihelion in early January.
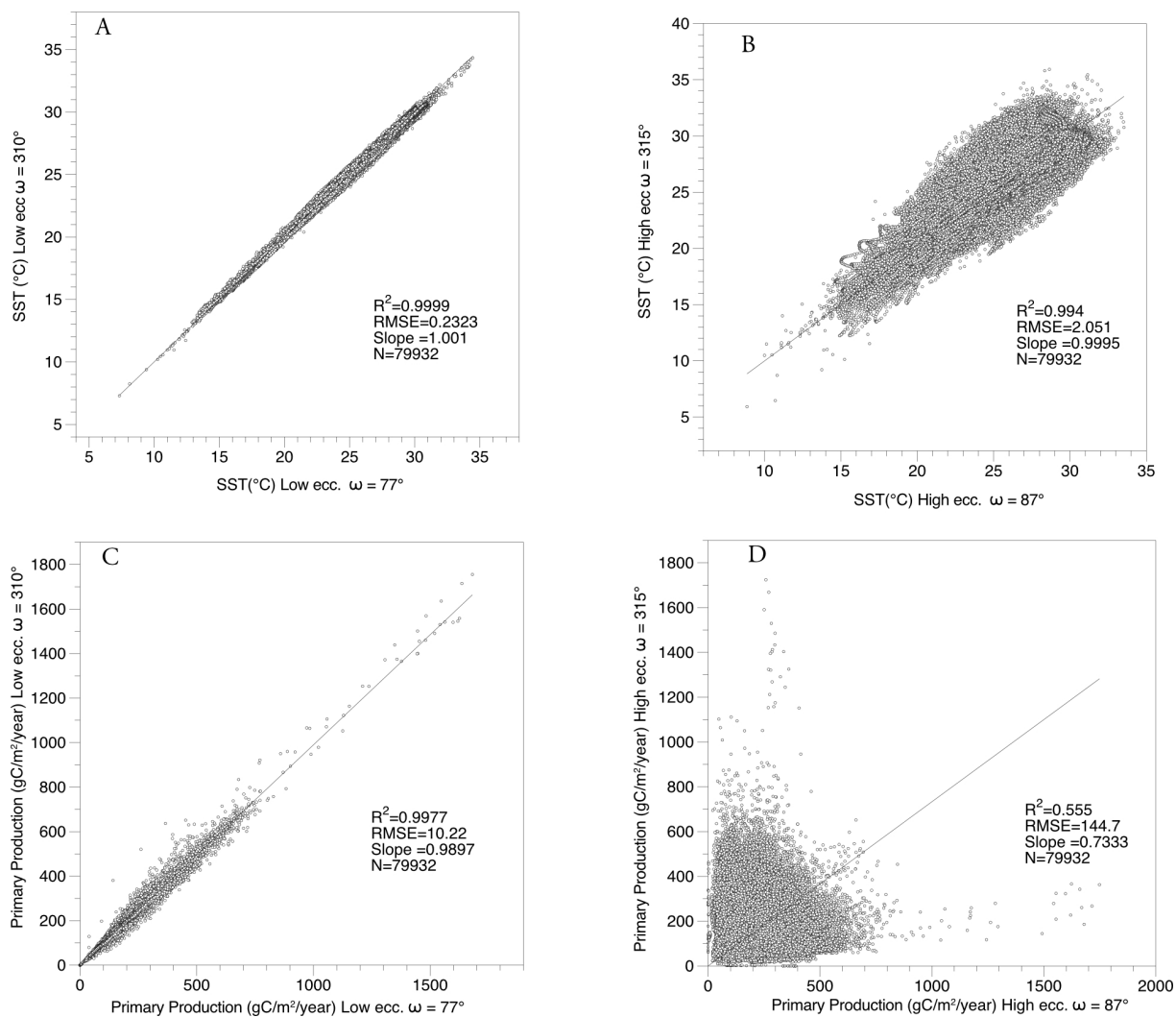
Figure 2. Correlation between Simulations at Opposite Precession Phases—Low (A and C) and High (B and D) Eccentricity—for Sea Surface Temperature (SST) (A and B) and Primary Productivity (PP) (C and D) across the Tropical Ocean Band (30°N-30°S, 6661 pixels) throughout Twelve Months. Each comparison is based on a total of 79,932 data points.
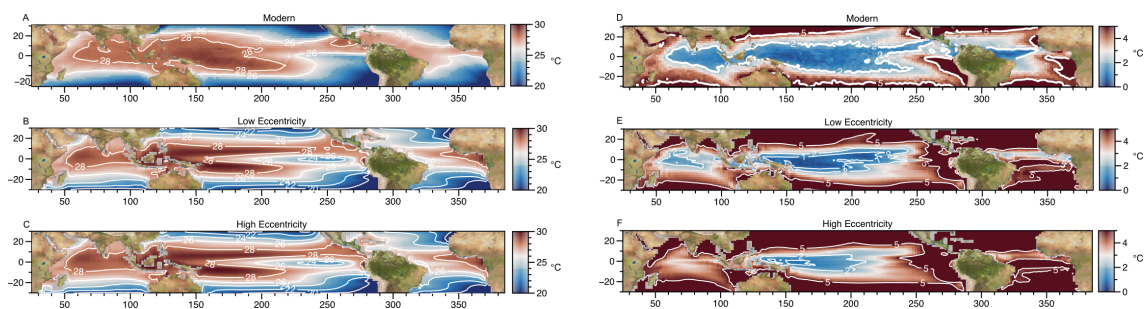
Figure 3. Sea surface temperature annual mean (A, B, C) and annual amplitude (D, E, F) from modern data (COADS) (A, D), from the simulation with low eccentricity (ω =310°) (B,E) and from the average of the 6 simulations with high eccentricity (C, F).
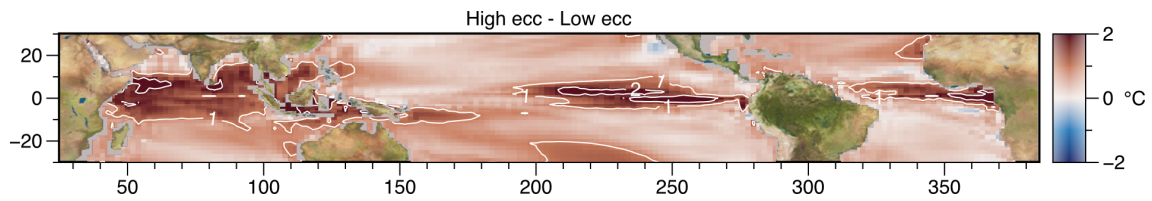
Figure 4. Difference in the SST amplitudes between the average of the 6 high eccentricity simulations and the low eccentricity simulation ($\omega =310°$)
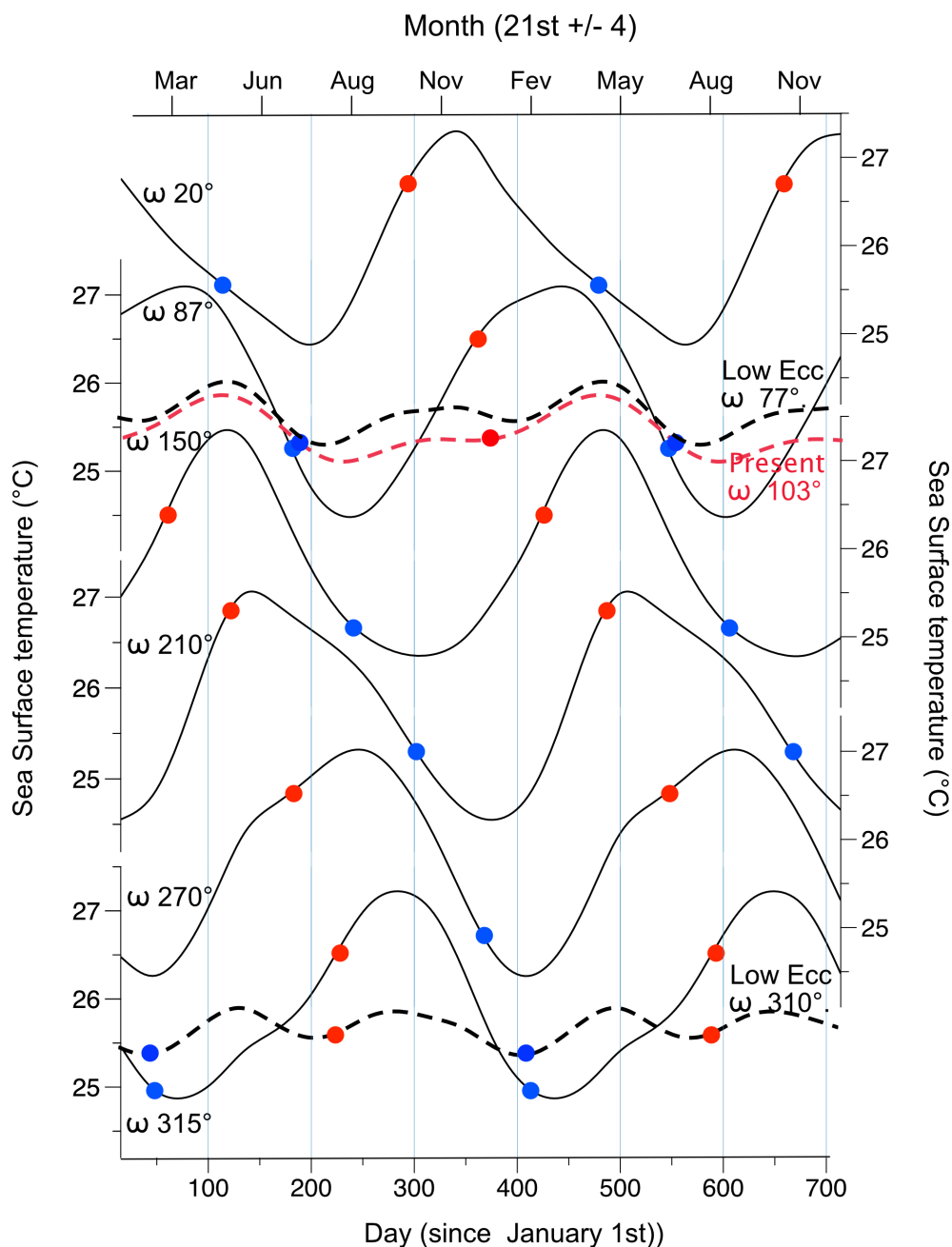
Figure 5. Two years series of SST between 30°N and 30°S from high eccentricity simulations (solid lines), from low eccentricity simulations (black dotted line) and from modern data (red dotted line). The longitude of the perihelion (ω) is indicated. The red dots represent the date of perihelion, and the blue dots that of the apehelion.
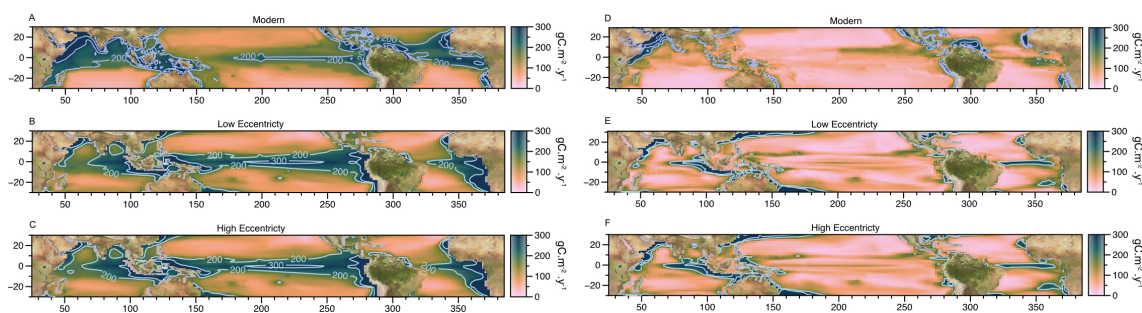
Figure 6. Primary production annual mean (A, B, C) and annual amplitude (D, E, F) from modern data (Satellite MODIS) (A, D), from the simulation with low eccentricity (ω =315°) (B,E) and from the average of the 6 simulations with high eccentricity (C, F).
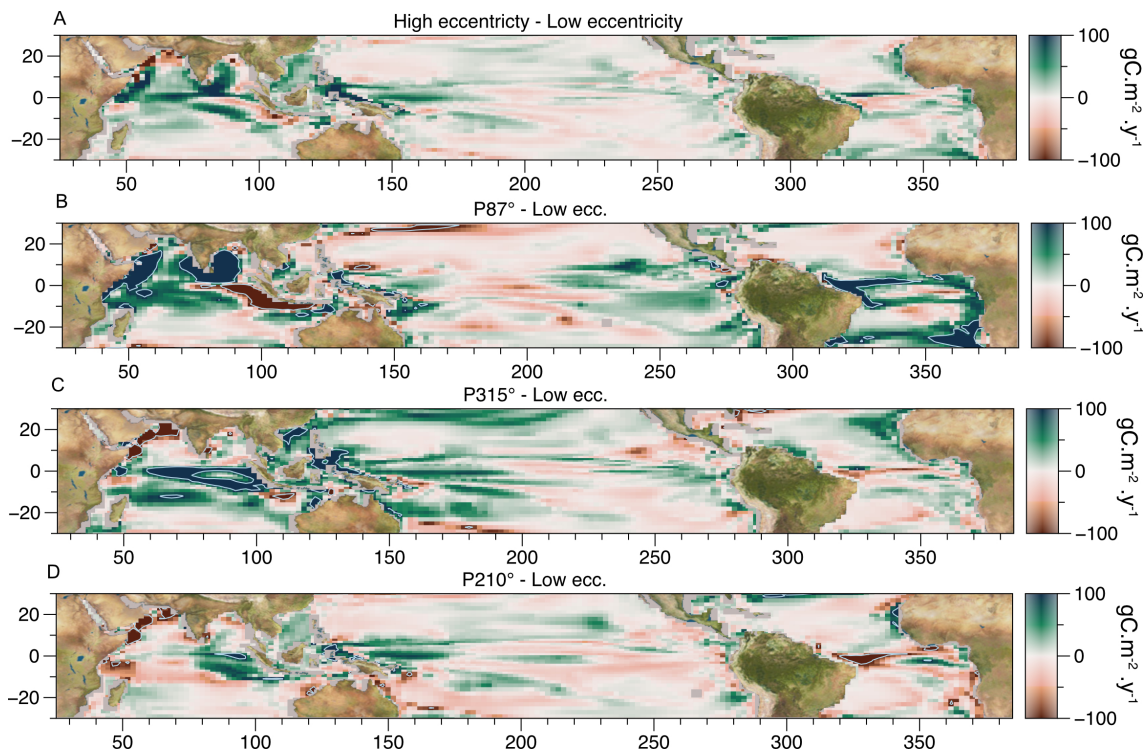
Figure 7. Difference of annual amplitude of primary production between high (A: average of the 6 simulations; B : simulation with ω =87°; C: simulation with ω =315°; D: simulation with ω =210°) and low eccentricity simulations with ω =310°.
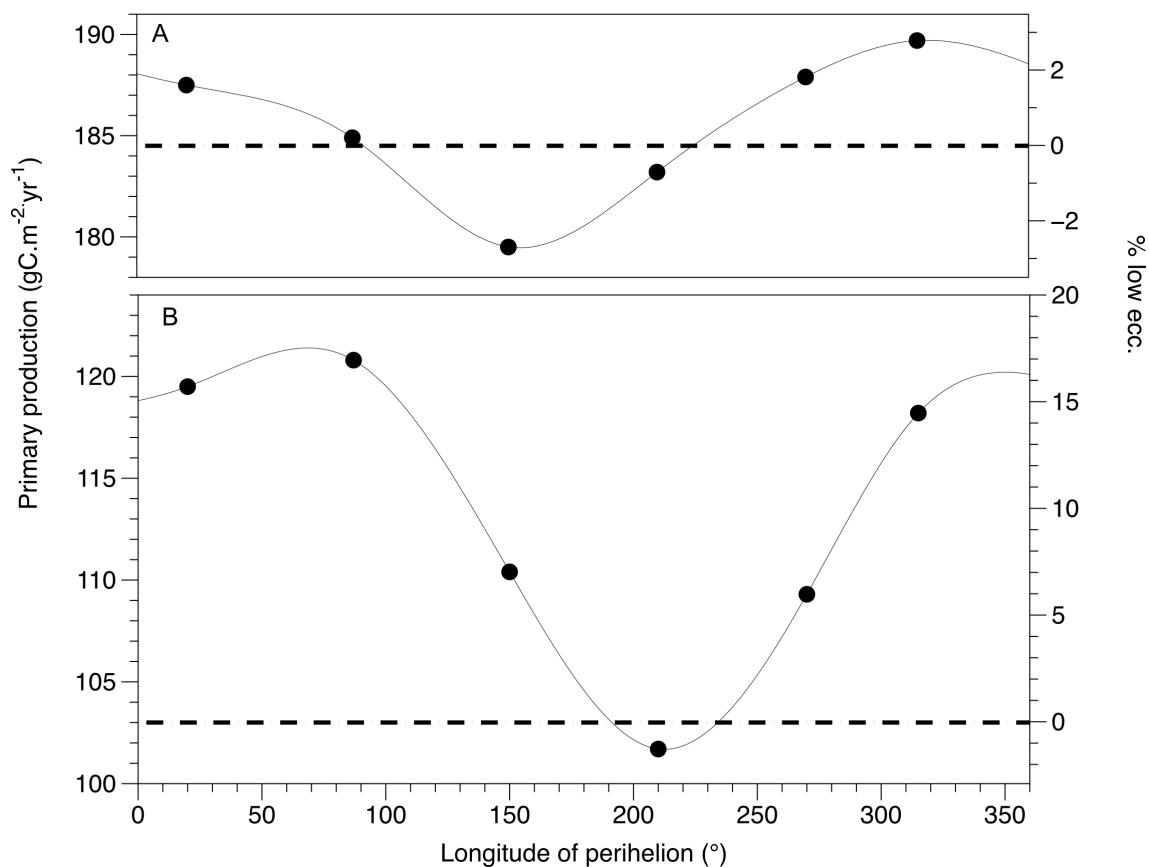
Figure 8. Figure 8 : Evolution of primary production annual mean (A) and annual amplitude (B) between 30°N and 30°S during a precession cycle for high eccentricity (solid line - dots : simulations) and low eccentricity (dotted line), left scale in : gC.m-2.yr-1, right scale in percentage relative to low eccentricity.
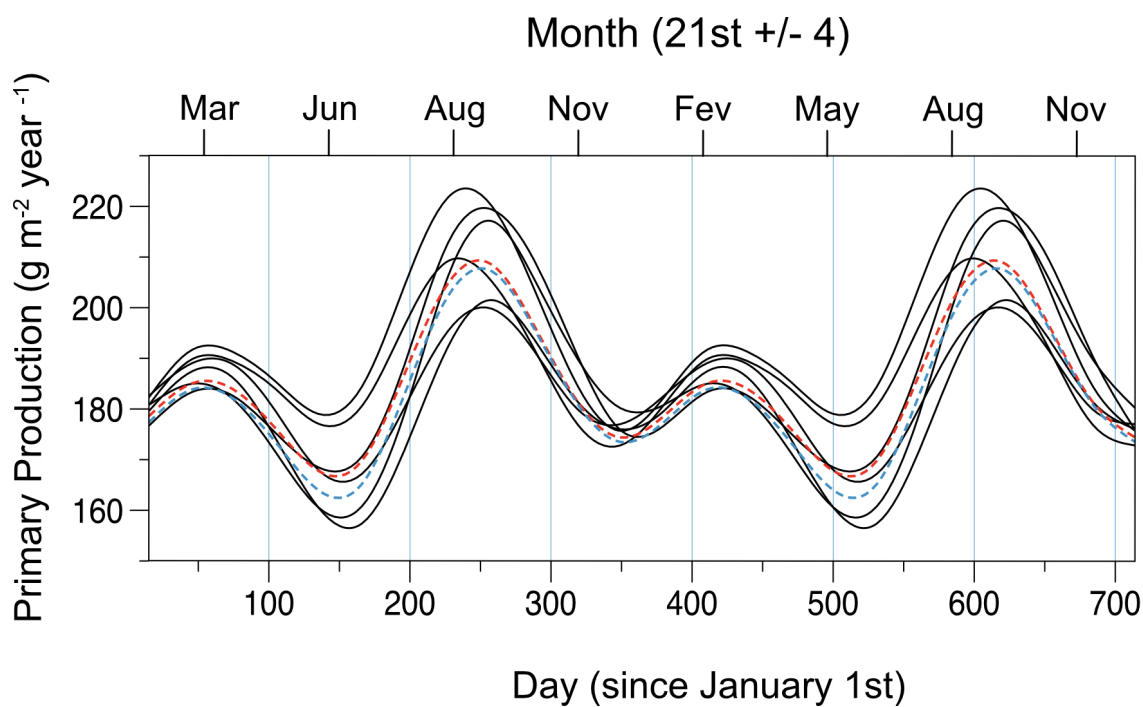
Figure 9. Two years series of primary production between 30°N and 30°S from high eccentricity simulations (solid lines) and low eccentricity simulation (red (ω =310°) and blue (ω =77°) dotted lines).
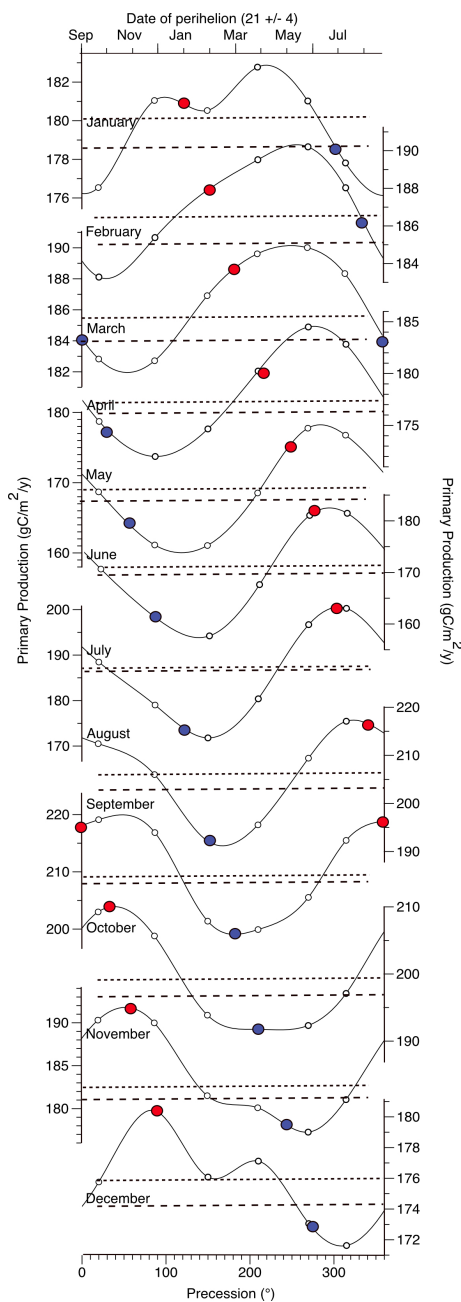
Figure 10. Monthly evolution of primary production at Low latitudes (30°N-30°S) during a precession cycle simulated at high eccentricity (solid line) from January (top) to December (bottom). The values simulated by the low experiments are in dotted line (ω =77°) and dashed line (ω =310°) to express the range of variation during a precession cycle at low eccentricity. Color dots correspond to the position of the perihelion (red) and aphelion (blue) when in occurs in the same month.
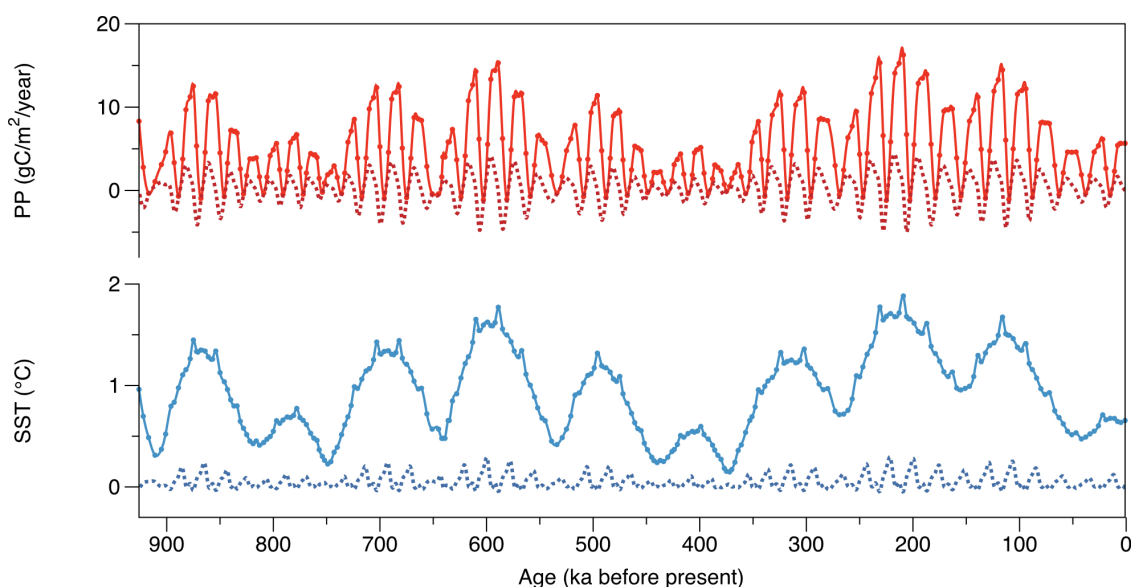
Figure 11. Simulated low-latitude ocean over a 900,000-year period, forced only by changing eccentricity and precession. The figure depicts SST (blue-bottom) and PP (red-top) in terms of annual mean (dotted lines) and annual amplitude (solid lines with dots). The 30°N-30°S average values for each of the six high eccentricity simulations, adjusted by subtracting the low eccentricity simulation ($\omega = 315°$) value, are arranged chronologically on a time frame based on precession (Laskar et al., 2004) for the last 900,000 years. These values are further scaled by the eccentricity for each time point, as represented by the equation $Y_t = (HE_\omega - LE).e_t/0.053$. Here, Y_t represents the value at time t, $HE\omega$ denotes the simulated value for a given perihelion longitude (ω) under high eccentricity, LE signifies the simulated value under low eccentricity ($\omega = 310°$), e_t represents the eccentricity at time t, and 0.053 corresponds to the eccentricity value used for the high eccentricity simulation.
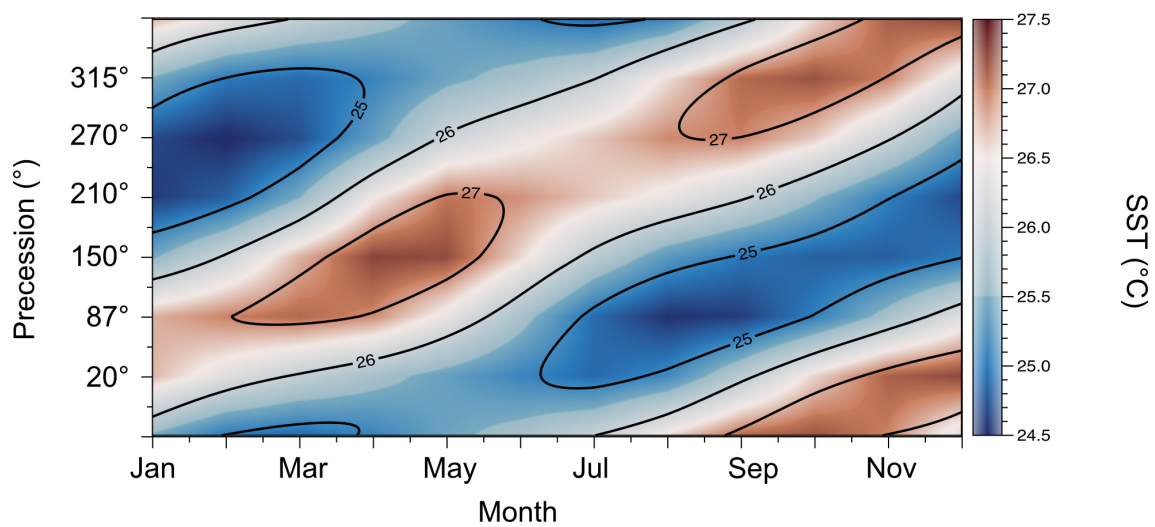
Figure 12. Low-latitude (30°N-30°S) annual variations of SST, along a precession cycle when eccentricity is high
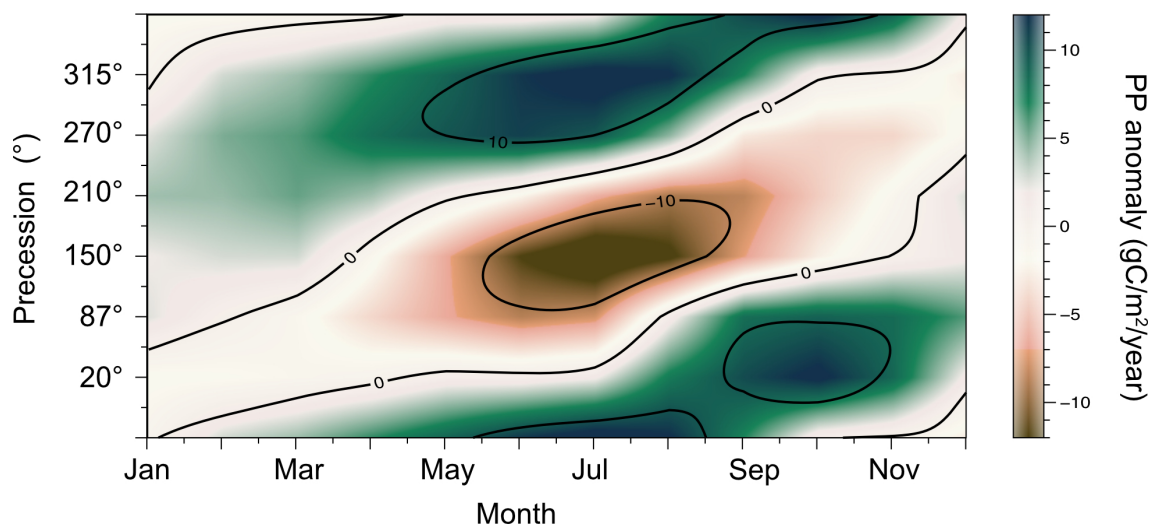
Figure 13. Low-latitude (30°N-30°S) annual variations of PP anomalies in high eccentricity relative to low eccentricity (ω =310°) along a precession cycle.
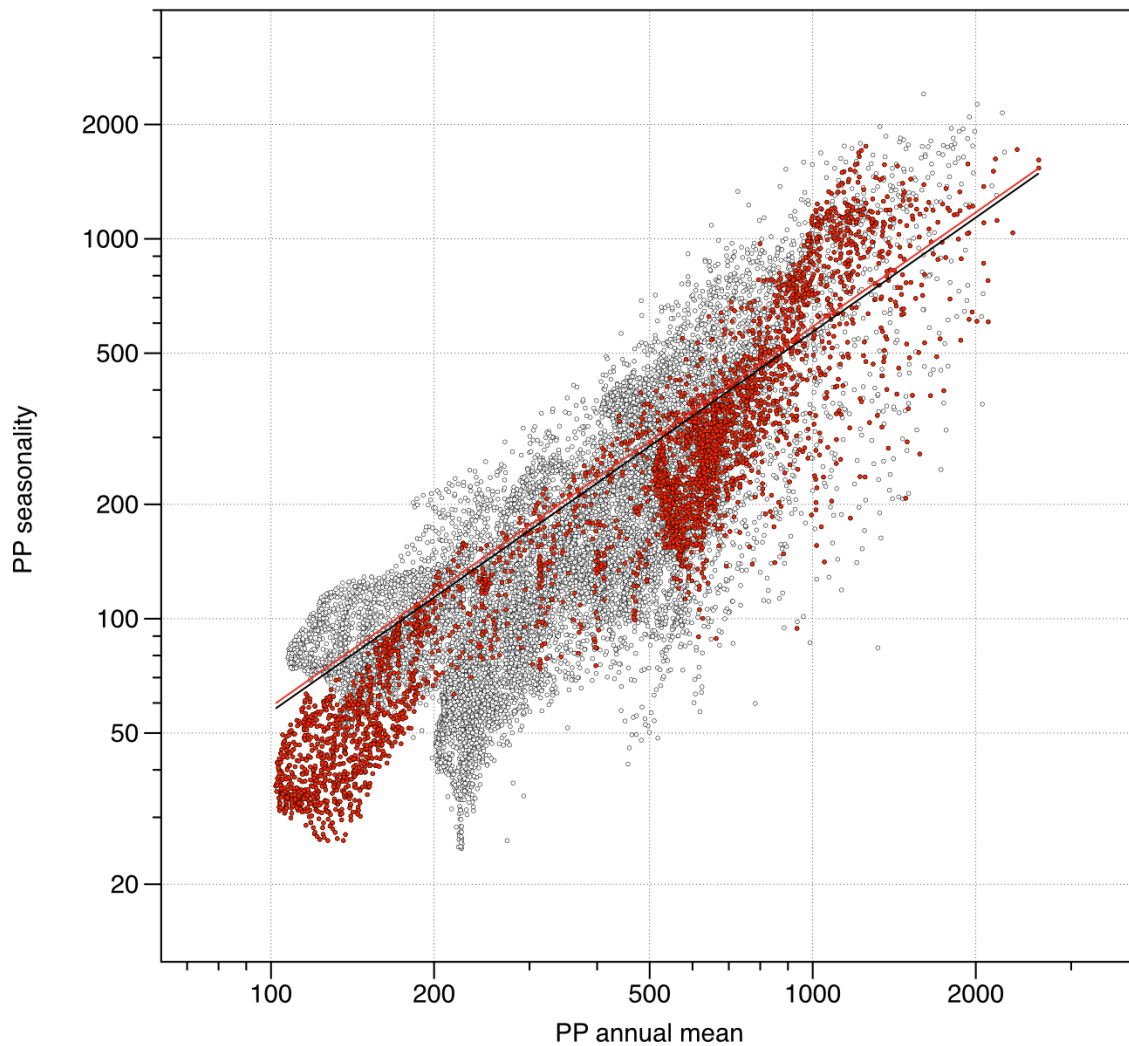
Figure 14. Figure 14: Relation between annual mean and annual amplitude (month max -month min) of primary production in the modern low latitudes (30°N-30°S) (Indian ocean values in red) from MODIS satellite imagery (Slutz et al., 1985). Black (all oceans) and red (Indian) lines represent the intercept free regressions (All : N= 16981, R^2 = 0.82, slope = 0.57, Indian : N = 3532, R^2 = 0.85, slope =0.59))
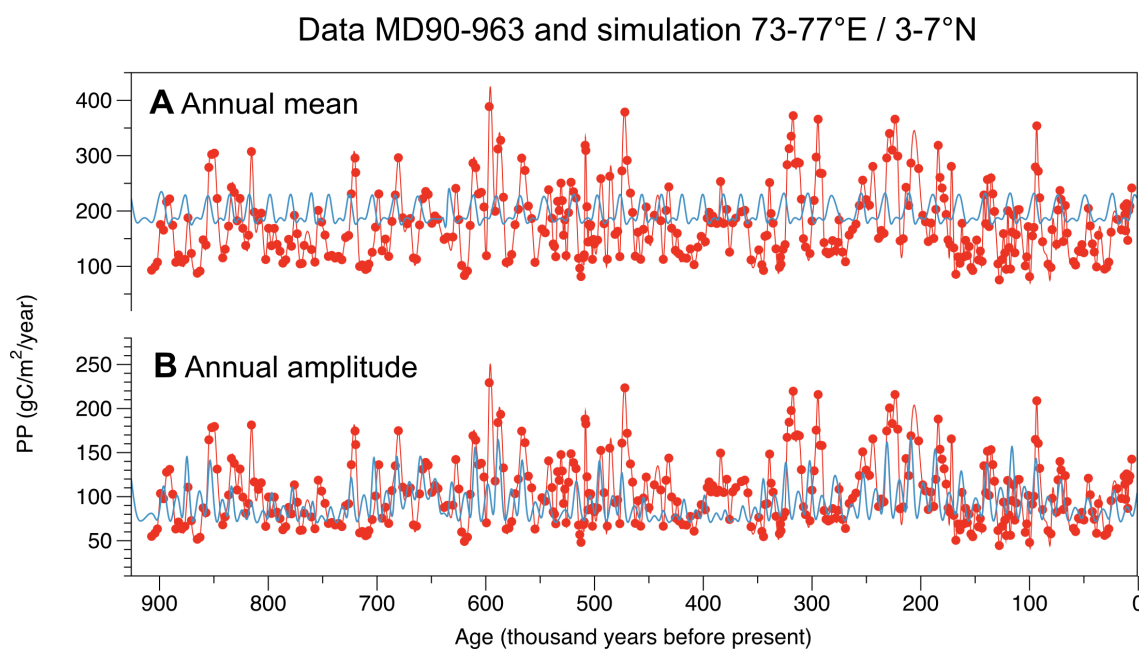
Figure 15. 900 kyr time series of annual (A) and amplitude (B) primary production in the Indian ocean at 75°E – 5°N (± 2°). Methods to construct the transient simulations (blue) are the same as figure 12. The estimated annual mean PP data (red) are from Core MD90-963 (Beaufort et al., 1997). In B, the annual mean PP data have been scaled by 0.59 to represent the seasonal PP (see Figure 14)

Configuration name	Eccentricity	Longitude of perihelion (°)	Month at perihelion	Obliquity	Annually averaged solar irradiance (W/m2)	Annual amplitude (W/m2)	Reference
Ecc. min - P310	0.005	310	August	23.45	329.2	38.5	Beaufort et al., 2022
Ecc. min - P77	0.006	77	December	23.74	328.7	36.5	Beaufort et al., 2022
Ecc. Max - P20	0.054	20	October	23.73	329.5	78.9	This work
Ecc. Max- P87	0.054	87	December	23.73	329.2	73.8	Beaufort et al., 2022
Ecc. Max - P210	0.054	150	March	23.73	328.7	93.9	This work
Ecc. Max - P210	0.054	210	May	23.73	329.1	101.7	This work
Ecc. Max - P270	0.054	270	July	23.73	328.9	89.2	This work
Ecc. Max - P315	0.053	315	August	23.84	329.1	82.7	Beaufort et al., 2022

Table 1: Summary of orbital parameters used for each simulation and annually averaged solar irradiance and its annual amplitude